Journal of Materials Chemistry A

ROYAL SOCIETY OF CHEMISTRY

PAPER

View Article Online
View Journal

Cite this: DOI: 10.1039/d5ta10602h

High capacity metal-rich copper sulfide as an intercalation-type cathode material for all solid-state batteries

Joonhyeok Park,†[a] Hyunjung Park,†[b] Seungmin Han,[a] Seungwoo Lee,[a] Jiseok Kwon,[a] Jeongheon Kim,[a] Jun Lim,[c] Ungyu Paik *[a] and Taeseup Song *[ac]

All solid-state batteries (ASSBs) employing sulfide-based electrolytes have attracted great attention as emerging energy storage systems due to high safety, high energy density, broad operating temperatures, *etc*. However, the introduction of sulfide-based solid electrolytes causes interfacial side-reactions with cathode/anode materials, resulting in electrochemical degradation. Here, we report a new intercalation-type $Cu_{1.8}S$ cathode material with a high capacity and interfacial compatibility for ASSBs. Compared to metal sulfides (M_xS), copper sulfides only have metal-rich phases ($x \geq 1.6$) due to the unique oxidation state of +1, enabling no weak S–S bonds, all strong Cu–S bonds, and a structural rigidness upon intercalation of foreign atoms. As a starting material, spherical microparticles assembled from CuS nanocrystals are prepared by a solvothermal method. After calcination at 300 °C, the CuS granules are transformed to porous $Cu_{1.8}S$ microspheres with a particle size of 1–3 μm and a surface area of 1.4 m^2 g^{-1}. A $Cu_{1.8}S$-based cathode shows a charge/discharge capacity of 274 mAh g^{-1}, a capacity retention of 80% over 100 cycles, and a high-rate capability of ~190 mAh g^{-1} at 1C-rate in a potential window of 0.5–2.5 V *vs.* Li/Li^+, leading to 1.5 times higher energy density than that of the conventional $LiCoO_2$ cathode. In addition, it shows a suppressed side reaction and electrochemical compatibility with the sulfide-based electrolyte. The achievements open a new avenue for the potential use of copper sulfides as cathode materials for ASSBs.

Received 31st December 2025
Accepted 5th March 2026

DOI: 10.1039/d5ta10602h

rsc.li/materials-a

1. Introduction

All solid-state batteries are considered next generation rechargeable batteries due to benefits of high safety, high energy density, and wide operating temperatures compared to conventional LIBs.[1–3] Replacing flammable liquid electrolytes with solid-state electrolytes not only prevents both explosion and fire but also increases the possibility for the use of Li-metal anodes, which makes ASSBs the most promising candidate for electric vehicles. This can be realized by the development of various solid electrolytes such as oxide-, sulfide-, and organic/inorganic-based electrolytes.[4–6] Among them, sulfide-based electrolytes such as Li_2S–P_2S_5, $Li_{4-x}Ge_{1-x}P_xS_4$, $Li_{10}GeP_2S_{12}$, *etc*. have relatively low grain boundary resistance and a high Li^+ ionic conductivity of ~10^{-3} S cm^{-1} equivalent to those of conventional liquid electrolytes at room temperature.[7,8] However, sulfide-based solid electrolytes cause interfacial side reactions with electrode materials. For a cathode material, niobium oxide (NbO_x) is coated as a protective layer on the surface of lithium transition metal oxides such as $LiCoO_2$. The preparation of the protective layers is a costly and time-consuming process. In addition, thiophosphate-based electrolytes have a narrow operating window of 1.6–2.3 V *vs.* Li/Li^+ and could be reduced above the redox potential of lithium metal (0 V) and oxidized below that of lithium transition metal oxides (~3.6 V for $LiCoO_2$). This is supported by the first-principles calculation and experimental evidence on decomposed products of lithium compounds such as Li_2S, Li_3P, Li_xGe, *etc*., resulting in a gradual degradation of electrochemical performances.[9–11] In this respect, the development of new electrode materials with physicochemical compatibility is highly recommended for ASSBs.

To use lithium metal anodes, conversion-type metal chalcogenides as the cathode materials were explored in the early stage of the development of lithium batteries employing liquid electrolytes.[12,13] Despite their high capacities, they suffer from poor cyclability due to the phase transition, reforming, and volume change upon cycling. After that, the intercalation-type titanium disulfide (TiS_2) appeared. Despite its stable operation, it encountered the shortcomings of low energy density

[a]*Department of Energy Engineering, Hanyang University, 222 Wangsimni-ro, Seoul, 04763, Republic of Korea. E-mail: upaik@hanyang.ac.kr; tssong@hanyang.ac.kr*

[b]*Department of Materials Science and Engineering, Chosun University, 146 Chosundae-gil, Gwangju, 61452, Republic of Korea*

[c]*Department of Battery Engineering, Hanyang University, 222 Wangsimni-ro, Seoul, 04763, Republic of Korea*

† These authors contributed equally to this work.

originating from the narrow operating voltage window of 1.7–2.5 V *vs.* Li/Li^+ and the limited amount of lithium insertion ($xLi + TiS_2 \leftrightarrow Li_xTiS_2$, $0 \leq x \leq 1$).[14,15] Moreover, uneven lithium plating/stripping and dendritic growth is another critical issue in the Li-metal/liquid electrolyte system.[13,16] Since the commercialization of Li-ion batteries with the $LiCoO_2$/C combination, various metal sulfides have been intensively studied as electrode materials.[17–28] However, most of them experience electrochemical irreversibility due to the following reasons: (1) decomposition and phase transformation during the galvanic reaction, (2) potential dissolution of sulfur atoms due to weak bond strength, and (3) chemical incompatibility with organic liquid electrolytes.

Copper sulfides have various polymorphs with a wide range of Cu to S ratios, Cu_xS ($0.5 \leq x \leq 2.0$). Among them, metal-rich phases ($x > 1.5$) such as chalcocite (Cu_2S),[29] djurleite ($Cu_{1.94}S$),[30] digenite ($Cu_{1.8}S$),[31,32] and anilite ($Cu_{1.75}S$)[33] are unique. These formulae are only found in group 11 metal (Cu, Ag, and Au) sulfides due to the +1 common oxidation state and enable a higher capacity than metal-deficient sulfides due to multiple redox couples. They were experimentally proven to be stable compounds from their crystallographic studies, refinement analyses, and electrochemical experiments. Specifically, they consist of all direct Cu–S bonds without weaker S–S bonds in their unit cells, resulting in enhanced structural stability and preventing reorganization of the anion frame during the entry of foreign metal cations into the lattice.[34] According to our previous study, it was confirmed that the $Cu_{1.8}S$ reversibly intercalates and deintercalates 1.4 Na^+ ions in the voltage range of 0.5–2.2 V *vs.* Na/Na^+.[35] Besides, copper sulfides with structural rigidness are likely to have chemical compatibility with sulfide-based electrolytes and prevent undesirable side reactions. Hence, all these merits are worth exploring the metal-rich Cu_xS as new cathode materials for ASSBs.

Here we first report hierarchical porous $Cu_{1.8}S$ microspheres as a new cathode material with promising electrochemical properties for ASSBs employing sulfide-based electrolytes. As a starting material, CuS/S composite microspheres are synthesized by the solvothermal method. To obtain a target material of the $Cu_{1.8}S$ phase, the composite microspheres are calcined at various temperatures in the range of 200–800 °C. As-prepared hierarchical porous CuS/$Cu_{1.8}S$/Cu_2S microspheres (denoted as HP-CuS MS, HP-$Cu_{1.8}S$ MS, and HP-Cu_2S MS, respectively) are characterized by various analytical tools to study their intrinsic properties. Superior electrochemical properties of the HP-Cu1.8S MS-based cathode are investigated by full-cell tests. Moreover, structural and chemical stability of Cu1.8S are examined through *ex situ* X-ray diffraction (XRD) and X-ray photoelectron spectroscopy (XPS).

2. Experimental

2.1. Synthesis of CuS/S composite microspheres

The CuS/S composite microspheres were prepared by a solvothermal method. 8 mmol of $Cu(NO_3)_2 \cdot 3H_2O$ was dissolved in 50 ml of dimethyl sulfoxide (DMSO) to form a clear solution. Then, 0.8 g of poly(vinyl pyrrolidone) (PVP, $M_w = 360\,000$) and 8 mmol of thiourea were added to this solution under stirring. Afterwards, the solution was transferred into an 80 ml Teflon-lined stainless-steel autoclave. The autoclave was sealed and kept at 120 °C for 20 h. After cooling down to room temperature, a black solid product was obtained by centrifuging the mixture. Then, powders were washed with deionized water and ethanol several times and dried at 80 °C overnight.

2.2. Synthesis of hierarchical porous copper sulfide microspheres

The CuS/S composite microspheres were placed in an alumina crucible and calcined at different temperatures of 200, 400, and 800 °C in argon gas for 5 h (a heating rate of 5 °C min^{-1}) in a horizontal tube furnace.

2.3. Material characterization

The morphologies of as-prepared powders were characterized by field-emission scanning electron microscopy (FE-SEM, JEOL JSM07600F), Cryo FIB-SEM (NFEC-2025-03-304629) and transmission electron microscopy (TEM, JEOL NEO ARM). Element mapping was carried out with an electron-probe microanalyzer (JXA-8100, JEOL). X-ray diffraction patterns of the samples were obtained by using an X-ray diffraction analyzer (XRD, Rigaku D/MAX RINT-2000). The nitrogen adsorption isotherm and pore size distribution were measured using a porosity instrument (BET, Micromeritics Tristar ||). X-ray photoelectron spectrometry (XPS, VG Microtech ESCA2000) was used for the analysis of the oxidation states.

2.4. Evaluation of electrochemical properties

For the full cell, 150 mg of the Li_6PS_5Cl electrolyte was placed in polycarbonate tube with a diameter of 13 mm and pressed by using a pelletizer under 300 MPa. The Li metal was attached on one side of the solid electrolyte and 15 mg cm^{-2} of the $Cu_{1.8}S$ microsphere composite ($Cu_{1.8}S$: SE : carbon additive = 50 : 45 : 5) was placed on the opposite side of the solid electrolyte and pressed by using a pelletizer under 50 MPa. The electrode density of the $Cu_{1.8}S$ composite cathode was approximately 1.8 g cm^{-3}. Then, the as-prepared full-cell was pressed under 20 MPa. For the full cell, the cathode material was prepared by mixing $LiNbO_3$ coated $LiCoO_2$ powders (Sigma-Aldrich, 99.8% trace metals basis) and the Li_6PS_5Cl electrolyte in a weight ratio of 70 : 30 using an agate mortar. 15 mg cm^{-2} of $LiCoO_2$ cathode composite powder was spread on one side of the as-prepared Li_6PS_5Cl electrolyte pellet in the polycarbonate tube and pressed under 300 MPa. Then, the Li metal-based anodes were attached on the opposite side of the electrolyte and pressed under 50 MPa. The electrode density of the $LiCoO_2$ cathode was approximately 2.0 g cm^{-3}. The as-prepared full cell was put into a pressed-type cell. All the processes were performed in a dry argon filled glovebox. Electrochemical performances of all the samples were analyzed by using a TOSCAT 3000 battery tester under the 20 MPa condition (TOSCAT 3000, Toyo systems, Tokyo Japan).

3. Results and discussion

As-prepared copper sulfide hax a spherical shape and a particle size in the range of 1–3 μm (Fig. S1a and b). XRD patterns confirmed that the microspheres are a composite of a CuS phase with a hexagonal structure (ICDD no. 06-0464) and the synthesized sulfur (marked by ▼, ICDD no. 08-0247) (Fig. S2a). The high-magnification SEM image shows that the CuS/S composite consists of CuS nanocrystals with a length of ~100 nm and a smooth region of residual sulfur (Fig. S2b). To achieve hierarchically porous Cu_xS microspheres, the post-calcination processes were conducted in a broad temperature range of 200–800 °C. SEM images in Fig. 1 demonstrate that they maintained the initial shape and the overall dimension, but exhibit different degrees of porosity and microstructures due to phase transitions and crystal growths during calcination at 200 °C (Fig. 1a and b), 400 °C (Fig. 1e and f), and 800 °C (Fig. 1i and j). HR-TEM images show lattice fringes of 0.19, 0.20, and 0.24 nm, corresponding to (110) for CuS (Fig. 1c), (220) for $Cu_{1.8}S$ (Fig. 1g), and (034) for Cu_2S (Fig. 1k), respectively. Elemental maps that confirmed a homogeneous distribution of Cu (red) and S (green) elements through the microspheres after calcination at 200 °C (Fig. 1d), 400 °C (Fig. 1h), and 800 °C (Fig. 1l).

According to XRD analysis (Fig. S3), the CuS/S composite was transformed into a pure CuS phase without the synthesized sulfur after calcination at 200 °C. It should be noted that a (110) peak is the most dominant in comparison with the reference data with the (103) peak at 32° (black line). This indicates that the CuS crystals have a preferential growth direction, which is often observed in chemical reactions such as Ostwald refining, Kirdendall effect, hydrothermal method, *etc.* as a preferential adsorption of precursor molecules and/or nuclei on the surface and plane to minimize the energy of the entire system. Due to the growth orientation, individual nanoparticles have a pill-shaped morphology with ~100 nm length and ~20 nm diameter (Fig. 2a). A unit cell of CuS shows a prismatic structure in which there are 4 Cu atoms in tetrahedral sites and 2 atoms in triangular sites, and there exist 4 direct S–S bonds (disulfide, $(S_2)^{2-}$) near the middle of *c* axis (Fig. 2b). After calcination at 400 °C (red line), the covellite CuS phase was converted into a $Cu_{1.8}S$ phase with a cubic structure (ICDD no. 056-1256). It is worth mentioning that $Cu_{1.8}S$ shows the strongest peak of a (220) plane at ~46°, which is certainly influenced by the dominant (110) plane of the CuS. The $Cu_{1.8}S$ crystals have a plate-like structure with a slight larger dimension than that of CuS because of agglomeration and crystal growth (Fig. 2c). For a $Cu_{7.2}S_4$ (=$Cu_{1.8}S$) unit cell, it consists of all Cu–S bonds without direct S–S bonds, and 7.2 Cu atoms randomly occupy near tetrahedral interstitial sites, with 4 S atoms near the 4b Wyckoff position (1/2, 1/2, 1/2), as face-centered cubic (FCC) lattices (Fig. 2d). The XRD patterns obtained after calcination at 800 °C (blue line) were matched with those of a chalcocite Cu_2S phase with a monoclinic structure (ICDD no. 33-0490). It possesses a dominant (630) plane derived from the (220) plane of $Cu_{1.8}S$. But more dominant (034) and (106) planes appeared, which might be due to a monoclinic structure and a polyhedron geometry (Fig. 2e and f).

To investigate inner porosity of the microspheres, the focused ion beam (FIB) technique was used for ablation. Cross-section SEM images showed the formation of macropores from the surface to the center of the spheres by interconnection of

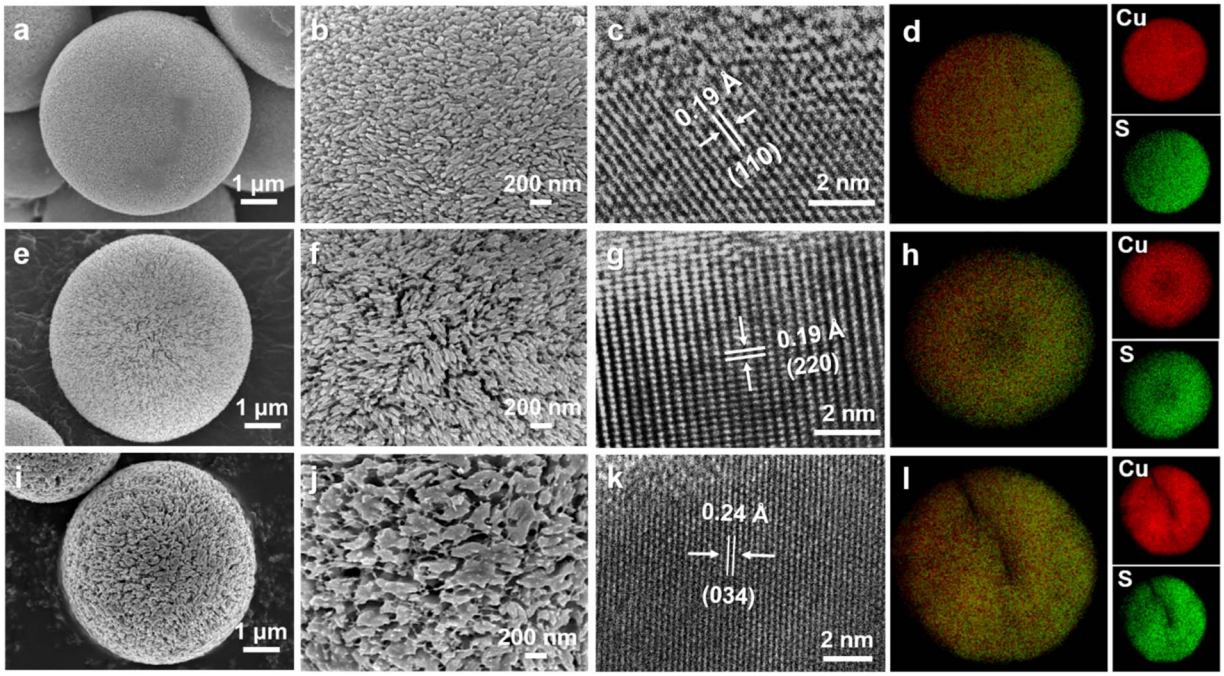

Fig. 1 Low- and high-magnification SEM images, high-resolution TEM image, and EDX map for copper and sulfur elements of copper sulfide microspheres after post-calcination at (a–d) 200 °C, (e–h) 400 °C, and (i–l) 800 °C.

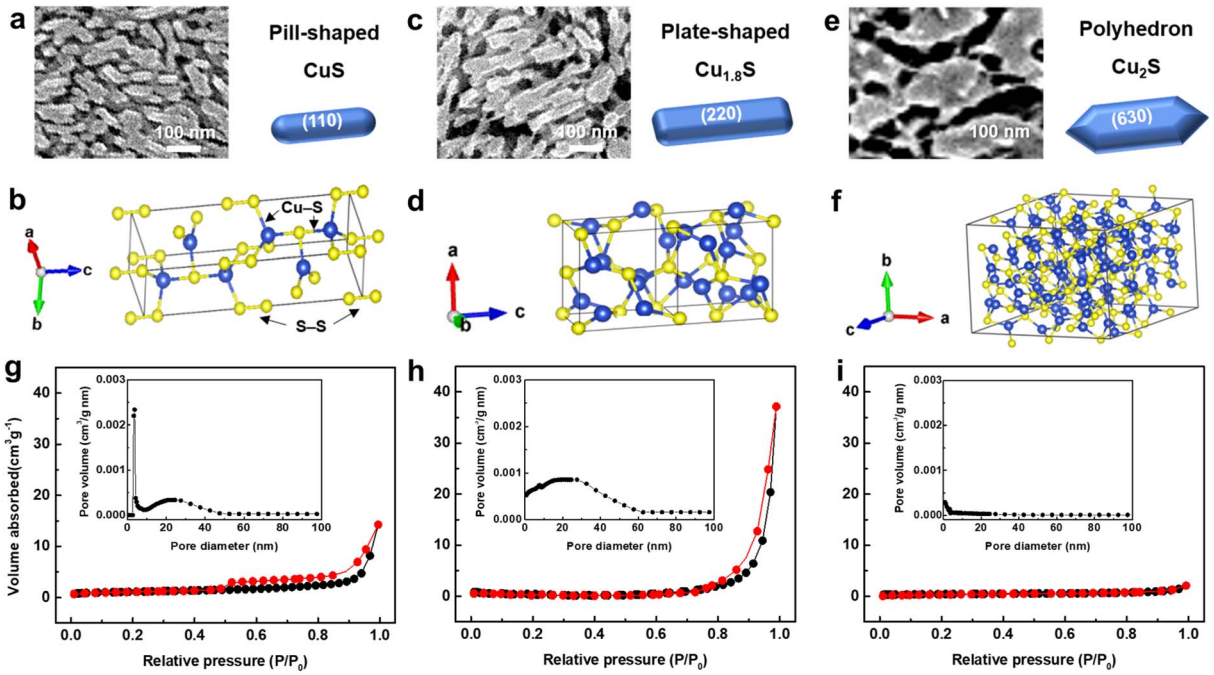

Fig. 2 High-magnification SEM images and crystallographic unit cells of (a and b) CuS, (c and d) $Cu_{1.8}S$, and (e and f) Cu_2S viewed along each of the <110>, <220>, and <630> directions. BET nitrogen adsorption–desorption isotherms and pore size distribution of (g) HP-CuS MS, (h) HP-$Cu_{1.8}S$ MS, and (i) HP-Cu_2S MS.

mesopores, as the calcination temperature increased, which demonstrates the formation of hierarchical porosity in the microspheres (Fig. S4). To study the surface area and a porosity of the microspheres, nitrogen (N_2) adsorption–desorption isotherms were obtained. Specific surface areas were determined to be ~3.9 $m^2\ g^{-1}$ for HP-CuS MS, 1.4 $m^2\ g^{-1}$ for HP-$Cu_{1.8}S$ MS, and 0.7 $m^2\ g^{-1}$ for HP-Cu_2S MS by the Brunauer–Emmett–Teller (BET) calculation. According to the International Union of Pure and Applied Chemistry (IUPAC) technical report,[36] HP-CuS MS exhibits usual type V isotherms with a type H_2 hysteresis loop. This is particularly observed in a solid with a complex pore structure and a network in a broad range of mesopore sizes, which is confirmed by two distinctive peaks in the mesopore range of 3–5 nm and 10–50 nm (Fig. 2g). HP-$Cu_{1.8}S$ MS has the same type V isotherm but a different H3 hysteresis-type loop. The pore size distribution indicates that the pores in the range of 3–5 nm disappeared due to the increase in pore size, which was confirmed by the SEM observation (Fig. 2h). In contrast, isotherms of HP-Cu_2S MS are classified as type III without a hysteresis loop which is typical of macroporous materials. No noticeable peaks were observed in the pore size distribution of 0–100 nm because macropores larger than 100 nm exceed the detectable maximum pore radius of 95 nm based on the Barrett–Joyner–Halenda (BJH) theory (Fig. 2i).

XPS spectra were analyzed to study chemical and electronic states of the three samples. All of them have a strong peak at ~931 eV assigned to Cu $2p_{3/2}$ with a +1 oxidation state (Fig. S5a). With phase transformation from CuS to Cu_2S *via* post-calcination, a shoulder peak centered at 933 eV become more prominent, which indicates an increase in the +2 oxidation state (Fig. S5a–c).[37] This change in the electronic state of Cu gave rise to a satellite near 942 eV often observed from materials with a d^9 electronic configuration in the ground state, which is another piece of evidence for the existence of Cu^{2+}.[38] This result agrees with previous reports that the oxidation state of copper in all sulfide compounds is usually a mixed valence of dominant Cu^{1+} and a small amount of Cu^{2+}.[39] A noticeable change was also observed in S 2p spectra (Fig. S6a–c). For the CuS sample at the bottom, it shows a broad peak with overlapping spin orbit doublets of disulfide ($(S_2)^{2-}$, 163.2 eV for $2p_{3/2}$ and 164.3 eV for $2p_{1/2}$) and monosulfide (S^{2-}, 161.6 eV for $2p_{3/2}$ and 162.6 eV for $2p_{1/2}$), respectively.[40] This is in good agreement with the existence of 4 disulfide and 2 monosulfide peaks in the unit cell structure of CuS. In contrast, the disulfide ($(S_2)^{2-}$) peaks significantly decreased for $Cu_{1.8}S$ and finally disappeared for the Cu_2S sample. The composition analyses are in accordance with the crystallographic study. It is deduced from the XPS result that the Cu_xS microspheres can possess multiple redox couples of $Cu^{0/1+}$ and $Cu^{1+/2+}$ as the active material. Area ratios of Cu^{1+} to Cu^{2+} for the three samples are calculated to be 0.9 to 0.1 (CuS), 0.79 to 0.21 ($Cu_{1.8}S$), and 0.71 to 0.28 (Cu_2S).

Based on the various characterization studies, the growth mechanism of hierarchically porous CuS, $Cu_{1.8}S$, and Cu_2S microspheres is proposed to be as follows; (1) formation of CuS nuclei in the presence of adsorbed thiourea and poly(vinyl pyrrolidone) during the solvothermal reaction, (2) crystal growth and self-assembly of CuS nanocrystals and synthesized sulfur, leading to the formation of CuS/S composite microspheres, (3) evaporation of residual sulfur and recrystallization

of CuS during post-calcination at 200 °C, and (4) phase transition from CuS to $Cu_{1.8}S$ to Cu_2S at the elevated temperatures of 400 and 800 °C, resulting in mesoporous and macroporous structures. Finally, the $Cu_{1.8}S$ microspheres as a cathode material were applied to ASSBs owing to the merits such as the Cu-rich phase, the highest porosity, and simple XRD patterns.

Prior to various evaluations of electrochemistry, a preliminary test was conducted to optimize a potential window for the $Cu_{1.8}S$-based cathode. While severe degradation of cyclability was observed upon discharging down to 0 V, a stable operation was achieved in the voltage range of 0.5–3.0 V *vs.* Li/Li^+ coupled with a Li anode (Fig. 3a and b). To investigate the phase evolution of $Cu_{1.8}S$, *ex situ* XRD measurements were conducted during cycling. As shown in Fig. 3c, $Cu_{1.8}S$ transforms into Cu_2S and Li_2S phases after lithiation, and the $Cu_{1.8}S$ phase reappears after delithiation. This result indicates that the reaction mechanism of $Cu_{1.8}S$ involves the intercalation of Li ions and a subsequent lattice rearrangement to form Cu_2S, rather than a conversion reaction that produces metallic Cu and Li_2S. Although sulfur in $Cu_{1.8}S$ reacts with Li to form Li_2S during lithiation, Cu_2S is preserved instead of being reduced to metallic Cu. Therefore, this intercalation-dominant mechanism is advantageous in mitigating the volume change typically observed in metal sulfides undergoing conversion reactions, thereby leading to enhanced electrochemical stability.

Full cell tests were conducted using two different positive materials such as the $LiCoO_2$-based cathode (LCO-BC) and the $Cu_{1.8}S$-based cathode (CS-BC), both coupled with the Li/In anode. Fig. 4a shows the initial voltage profiles of two cells at a current density of 0.05C. LCO-BC and the CS-BC give a specific charge/discharge capacity of 173/148 mAh g^{-1} and 519/503 mAh g^{-1} and coulombic efficiency of 86% and 97%, respectively. This high efficiency of CS-BC indicates great compatibility with the sulfide solid electrolyte and suppression of side reactions at the interface. Fig. 4b exhibits the energy densities of each cathode in terms of integral area under the discharge curve (0 V *vs.* Li/Li^+). It is worth noting that CS-BC exhibits not only higher discharge capacities but also much larger volumetric/gravimetric energy density than that of LCO-BC despite the lower operating potential window. The rate capability at various current densities was measured in the range of 0.05 to 1C (Fig. 4c). Despite lower capacity retentions, CS-BC shows superior discharge capacities to those of LCO-BC. Notably, CS-BC retains a capacity of ~190 mAh g^{-1} three times larger than 60 mAh g^{-1} of LCO-BC at the high current density of 1C. This superior discharge capacity of CS-BC at a high current density of 1C was also confirmed in tests using a Li metal anode (Fig. S7). Fig. 4d shows cycle performances and coulombic efficiencies of the two cells at a current density of 0.5C. Capacity retentions were 70% (89 mAh g^{-1}) for LCO-BC and 80% (274 mAh g^{-1}) for CS-BC over 100 cycles. Fig. 4e shows EIS spectra of two cells before/after cycles. Although both cells exhibited an increase in total resistance after cycling, the resistance increase in LCO-BC was significantly more pronounced compared to that of CS-BC.

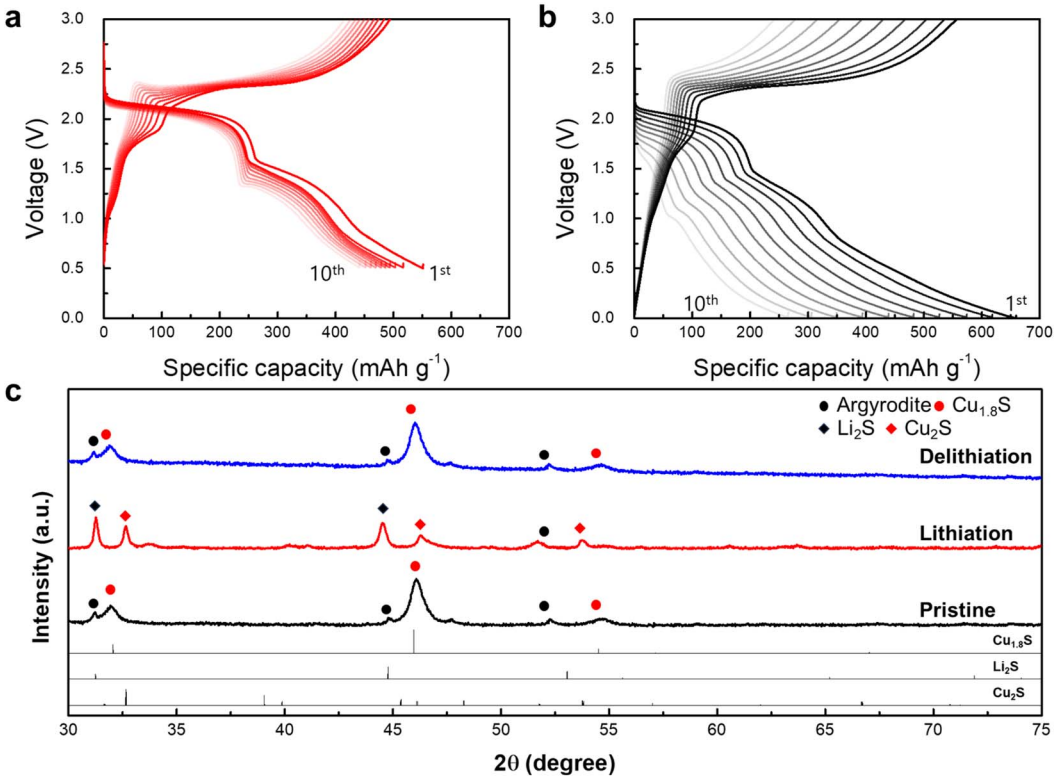

Fig. 3 Electrochemical properties of ASSBs using a $Cu_{1.8}S$-based cathode (CS-BC). Voltage profiles (1st to 10th cycles) for the ASSBs in the voltage range of (a) 0.5–3 V and (b) 0–3 V (*vs.* Li/Li+). (c) XRD patterns of the ASSB identifying the phase transformation of $Cu_{1.8}S$ during charging and discharging processes.

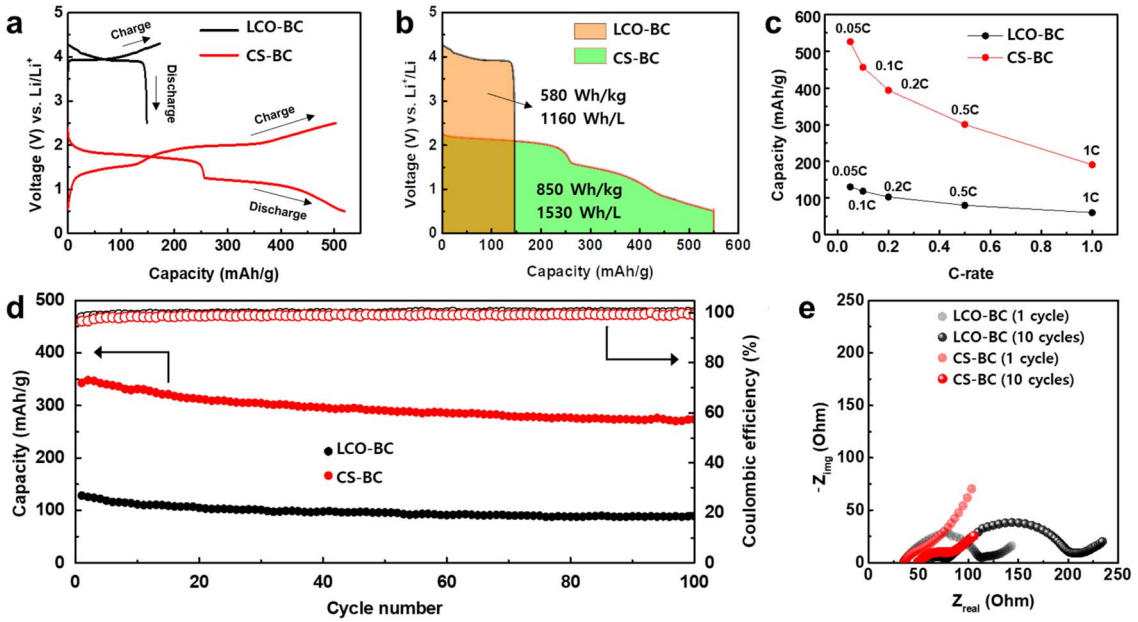

Fig. 4 Electrochemical properties of ASSBs using an $LiCoO_2$-based cathode (LCO-BC) and $Cu_{1.8}S$-based cathode (CS-BC) with a Li/In anode. (a) Initial voltage profiles for the ASSBs at 0.05C. (b) The energy densities of each cathode determined in terms of areas between the discharge curves and 0 V (*vs.* Li/Li^+). (c) Discharge capacities at current rates of 0.05, 0.1, 0.2, 0.5, and 1C. (d) Cycle performances for 100 cycles at 0.5C. (e) EIS spectra of ASSBs using LCO-BC and CS-BC after 1 and 10 cycles.

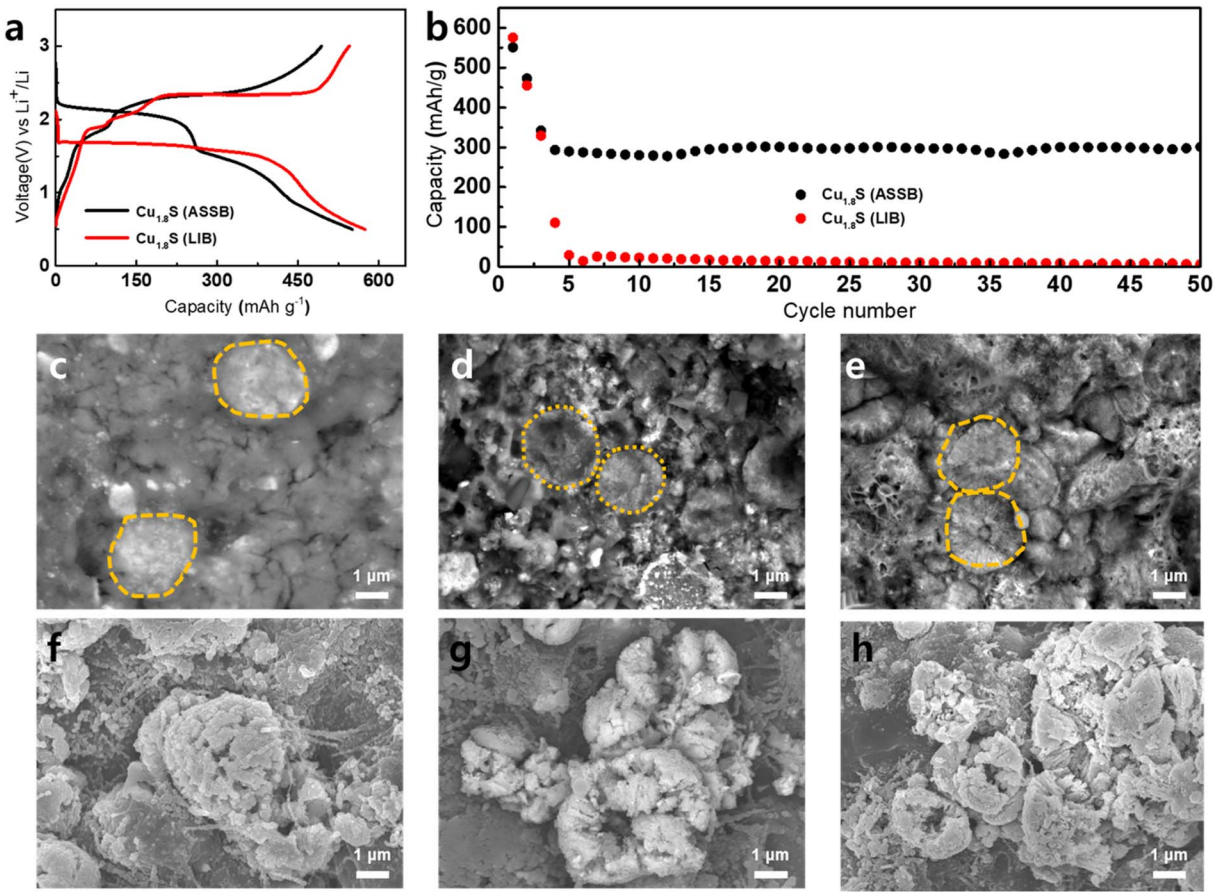

Fig. 5 Electrochemical properties of ASSBs and LIBs using an Cu1.8S-based cathode (CS-BC) with a Li metal anode. (a) Initial voltage profiles for the ASSBs and LIBs at 0.05C. (b) Cycle performances for 50 cycles at 0.5C. SEM images of CS-BC after 1, 10 and 50 cycles for (c–e) ASSBs and (f–h) LIBs.

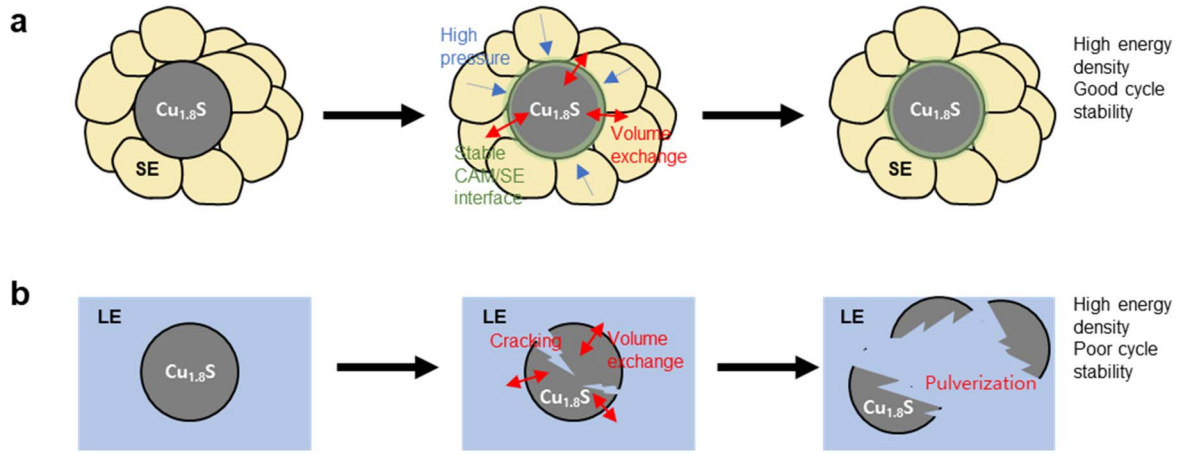

Fig. 6 Schematic of morphological and interfacial evolution of $Cu_{1.8}S$ during cycling in (a) ASSBs and (b) LIBs.

This substantial increase in LCO-BC is likely attributed to severe interfacial side reactions between the cathode and the sulfide-based electrolyte. These reactions lead to the decomposition of the argyrodite Li_6PS_5Cl electrolyte and the subsequent formation of lithium compounds with low ionic conductivity, such as Li_2S, Li_3P, and LiCl. To precisely analyze the resistance components of CS-BC, a distribution of relaxation times (DRT) analysis was performed on the EIS spectra (Fig. S8).[41] This approach allows for the deconvolution of overlapping electrochemical processes, clearly separating individual impedance contributions. In these profiles, five distinct peaks (P1 to P5) are observed in order of decreasing frequency. The peak at high frequency (P5) corresponds to the grain boundary resistance (R_{SE}). In the intermediate frequency region, P4, P3, and P2 denote the resistances from the solid electrolyte interphase (R_{SEI}), mechanical contact, and charge transfer (R_{ct}), respectively, while the low-frequency region (P1) reflects the Li-ion diffusion process (W_{diff}).[42–44] Based on the DRT analysis of CS-BC after 100 cycles, it was confirmed that all resistance components remained relatively stable (Fig. S9).

To prove the advantage of the $Cu_{1.8}S$ cathode for the ASSB, a cell test was performed using a LIB system. Fig. 5a shows the initial voltage profiles at a C-rate of 0.05C. The initial capacity of the LIB is higher than that of the ASSB owing to the better wettability and ionic conductivity of the liquid electrolyte. The liquid system exhibits a flat, single voltage plateau, which is believed to result from excellent wettability and fast ionic diffusion.[45] While the $Cu_{1.8}S$ cathode in the LIB system undergoes a rapid capacity fading, the one in the ASSB system shows superior cyclability in Fig. 5b (1–3rd formation: 0.05C–0.2C; 4–50th cycles: 0.5C). This result is ascribed to the effective suppression of cracking and pulverization of $Cu_{1.8}S$ in the ASSB. To verify this thesis, *ex situ* SEM images were obtained on electrodes after the 1st, 10th, and 50th cycles. For the ASSB, two distinct areas were observed; a porous region (the solid electrolyte) and a dense region ($Cu_{1.8}S$). As shown in Fig. 5c–e, the $Cu_{1.8}S$ spheres in the ASSB maintained their original structure up to 50 cycles. In contrast, the $Cu_{1.8}S$ particles still have the spherical shape but exhibit cracking and pulverization in the LIB system (Fig. 5f–h). EIS spectra were obtained during cycling (Fig. S10). The EIS spectra of the LIB system reveal a severe and continuous increase in the bulk and charge-transfer resistances.

Fig. 6 illustrates a schematic comparison of the morphological and interfacial evolution of the $Cu_{1.8}S$ cathode during cycling. In the ASSB system, all solid components and the cell configuration effectively suppress the volume change of $Cu_{1.8}S$, resulting in a stable interface and structural integrity (Fig. 6a). In contrast, the LIB system allows volume expansion of $Cu_{1.8}S$ toward the area of the liquid electrolyte, leading to severe particle cracking and pulverization (Fig. 6b). This mechanical degradation is the primary cause of the poor cycle life observed in LIBs. Consequently, $Cu_{1.8}S$ is a promising candidate as a high-energy-density cathode material specifically for next-generation ASSBs.

4. Conclusion

In summary, we successfully synthesized hierarchically porous $Cu_{1.8}S$ microspheres *via* a solvothermal method followed by calcination at 400 °C and demonstrated their potential as a high-performance cathode material for all-solid-state batteries (ASSBs) employing sulfide-based electrolytes. The unique crystallographic feature of the metal-rich $Cu_{1.8}S$ phase, characterized by the absence of weak S–S bonds and the presence of strong Cu–S bonds, provided inherent structural rigidity. Additionally, the hierarchical porosity of the microspheres effectively buffered the volume changes during cycling. The $Cu_{1.8}S$-based all-solid-state cell exhibited superior electrochemical performance compared to the conventional $LiCoO_2$ cathode. Crucially, the reaction mechanism study utilizing *ex situ* XRD and SEM revealed two key factors for this stability: (1) the lithiation process follows an intercalation-dominant mechanism rather than a conversion reaction, which mitigates excessive volume expansion. (2) The external pressure applied in the ASSB system effectively suppresses particle cracking and pulverization, which were identified as critical failure modes in liquid electrolyte systems. These findings

suggest that metal-rich copper sulfides, when combined with the mechanical confinement of ASSBs, offer a new and promising avenue for developing high-energy-density and chemically compatible cathode materials for next-generation energy storage systems.

Author contributions

J. P. and H. P. conceived the concept and analyzed the results. U. P. and T. S. supervised the project. J. P. and H. P. designed the experiments and wrote the manuscript with assistance from S. H. and S. L. J. K. and J. K. carried out materials characterization and electrochemical measurements. J. I. prepared the samples. All authors reviewed and commented on the manuscript.

Conflicts of interest

There are no conflicts to declare.

Data availability

The data supporting this article have been included as part of the supplementary information (SI). Supplementary information: XRD, SEM, XPS, voltage profiles, EIS, and DRT analysis. See DOI: https://doi.org/10.1039/d5ta10602h.

Acknowledgements

This work was supported by the National Research Foundation of Korea (NRF) grant funded by the Korean government (MSIT) (no. RS-2025-02233037).

References

1 U. Ulissi, M. Agostini, S. Ito, Y. Aihara and J. Hassoun, *Solid State Ionics*, 2016, **296**, 13–17.
2 T. Baba and Y. Kawamura, *Front. Energy Res.*, 2016, **4**, 22.
3 A. Hayashi, Y. Nishio, H. Kitaura and M. Tatsumisago, *Electrochem. Commun.*, 2008, **10**, 1860–1863.
4 A. Manthiram, X. W. Yu and S. F. Wang, *Nat. Rev. Mater.*, 2017, **2**, 16103.
5 R. C. Xu, X. L. Wang, S. Z. Zhang, Y. Xia, X. H. Xia, J. B. Wu and J. P. Tu, *J. Power Sources*, 2018, **374**, 107–112.
6 X. Y. Yao, B. X. Huang, J. Y. Yin, G. Peng, Z. Huang, C. Gao, D. Liu and X. X. Xu, *Chin. Phys. B*, 2016, 25.
7 F. Mizuno, A. Hayashi, K. Tadanaga and M. Tatsumisago, *Adv. Mater.*, 2005, **17**, 918.
8 N. Kamaya, K. Homma, Y. Yamakawa, M. Hirayama, R. Kanno, M. Yonemura, T. Kamiyama, Y. Kato, S. Hama, K. Kawamoto and A. Mitsui, *Nat. Mater.*, 2011, **10**, 682–686.
9 S. Wenzel, D. A. Weber, T. Leichtweiss, M. R. Busche, J. Sann and J. Janek, *Solid State Ionics*, 2016, **286**, 24–33.
10 S. Wenzel, S. Randau, T. Leichtweiß, D. A. Weber, J. Sann, W. G. Zeier and J. Janek, *Chem. Mater.*, 2016, **28**, 2400–2407.
11 Y. Zhu, X. He and Y. Mo, *ACS Appl. Mater. Interfaces*, 2015, **7**, 23685–23693.
12 M. Winter, B. Barnett and K. Xu, *Chem. Rev.*, 2018, **118**, 11433–11456.
13 J. Xie and Y.-C. Lu, *Nat. Commun.*, 2020, **11**, 2499.
14 M. S. Whittingham, *Chem. Rev.*, 2004, **104**, 4271–4302.
15 M. S. Whittingham, *Science*, 1976, **192**, 1126–1127.
16 J. M. Tarascon and M. Armand, *Nature*, 2001, **414**, 359–367.
17 D. W. Su, S. X. Dou and G. X. Wang, *Chem. Commun.*, 2014, **50**, 4192–4195.
18 X. Q. Xie, D. W. Su, S. Q. Chen, J. Q. Zhang, S. X. Dou and G. X. Wang, *Chem.–Asian J.*, 2014, **9**, 1611–1617.
19 L. David, R. Bhandavat and G. Singh, *ACS Nano*, 2014, **8**, 1759–1770.
20 Z. Shadike, M. H. Cao, F. Ding, L. Sang and Z. W. Fu, *Chem. Commun.*, 2015, **51**, 10486–10489.
21 S. H. Choi and Y. C. Kang, *Nanoscale*, 2015, **7**, 3965–3970.
22 G. D. Park, J. S. Cho and Y. C. Kang, *Nanoscale*, 2015, **7**, 16781–16788.
23 S. J. Peng, X. P. Han, L. L. Li, Z. Q. Zhu, F. Y. Cheng, M. Srinivansan, S. Adams and S. Ramakrishna, *Small*, 2016, **12**, 1359–1368.
24 Y. N. Ko and Y. C. Kang, *Carbon*, 2015, **94**, 85–90.
25 Y. X. Wang, J. P. Yang, S. L. Chou, H. K. Liu, W. X. Zhang, D. Y. Zhao and S. X. Dou, *Nat. Commun.*, 2015, **6**, 8689.
26 L. Wu, H. Y. Lu, L. F. Xiao, J. F. Qian, X. P. Ai, H. X. Yang and Y. L. Cao, *J. Mater. Chem. A*, 2014, **2**, 16424–16428.
27 Z. Zhang, Y. Q. Gan, Y. Q. Lai, X. D. Shi, W. Chen and J. Li, *RSC Adv.*, 2015, **5**, 103410–103413.
28 C. Q. Shang, S. M. Dong, S. L. Zhang, P. Hu, C. J. Zhang and G. L. Cui, *Electrochem. Commun.*, 2015, **50**, 24–27.
29 R. W. Potter, *Econ. Geol.*, 1977, **72**, 1524–1542.
30 H. T. Evans Jr, *Z. Kristallogr. - Cryst. Mater.*, 1979, **150**, 299–320.
31 G. Will, E. Hinze and A. R. M. Abdelrahman, *Eur. J. Mineral.*, 2002, **14**, 591–598.
32 W. C. Jiang, F. Wu, Y. J. Jiang, M. X. Sun, K. Zhang, Y. L. Xia, D. R. Wang and A. M. Xie, *Nanoscale*, 2017, **9**, 10961–10965.
33 K. Koto and N. Morimoto, *Acta Crystallogr., Sect. B*, 1970, **26**, 915–924.
34 Y. Xie, G. Bertoni, A. Riedinger, A. Sathya, M. Prato, S. Marras, R. Y. Tu, T. Pellegrino and L. Manna, *Chem. Mater.*, 2015, **27**, 7531–7537.
35 H. Park, J. Kwon, H. Choi, D. Shin, T. Song and X. W. D. Lou, *ACS Nano*, 2018, **12**, 2827–2837.
36 M. Thommes, K. Kaneko, A. V. Neimark, J. P. Olivier, F. Rodriguez-Reinoso, J. Rouquerol and K. S. W. Sing, *Pure Appl. Chem.*, 2015, **87**, 1051–1069.
37 M. D. Ye, X. R. Wen, N. Zhang, W. X. Guo, X. Y. Liu and C. J. Lin, *J. Mater. Chem. A*, 2015, **3**, 9595–9600.
38 J. Ghijsen, L. H. Tjeng, J. Vanelp, H. Eskes, J. Westerink, G. A. Sawatzky and M. T. Czyzyk, *Phys. Rev. B:Condens. Matter Mater. Phys.*, 1988, **38**, 11322–11330.
39 S. W. Goh, A. N. Buckley and R. N. Lamb, *Miner. Eng.*, 2006, **19**, 204–208.
40 J. C. W. Folmer and F. Jellinek, *J. Less-Common Met.*, 1980, **76**, 153–162.
41 J. Illig, M. Ender, T. Chrobak, J. P. Schmidt, D. Klotz and E. Ivers-Tiffée, *J. Electrochem. Soc.*, 2012, **159**, A952.

42 C.-Y. Yu, J. Choi, J. Dunham, R. Ghahremani, K. Liu, P. Lindemann, Z. Garver, D. Barchiesi, R. Farahati and J.-H. Kim, *J. Power Sources*, 2024, **597**, 234116.
43 J. W. Yap, T. Wang, H. Cho and J.-H. Kim, *Electrochim. Acta*, 2023, **446**, 142108.
44 C. Wei, D. Yu, X. Xu, R. Wang, J. Li, J. Lin, S. Chen, L. Zhang and C. Yu, *Chem.–Asian J.*, 2023, **18**, e202300304.
45 C.-H. Lai, K.-W. Huang, J.-H. Cheng, C.-Y. Lee, B.-J. Hwang and L.-J. Chen, *J. Mater. Chem.*, 2010, **20**, 6638–6645.